

Resonance Spin Flavour Precession and Solar Neutrinos

João Pulido ^{*} and E. Kh. Akhmedov [†]

*Centro de Física das Interações Fundamentais (CFIF)
Departamento de Física, Instituto Superior Técnico
Av. Rovisco Pais, P-1049-001 Lisboa, Portugal*

Abstract

We examine the prospects for the resonance spin flavour precession as a solution to the solar neutrino problem. We study seven different realistic solar magnetic field profiles and, by numerically integrating the evolution equations, perform a fit of the event rates for the three types of solar neutrino experiments (Ga, Cl and SuperKamiokande) and a fit of the energy spectrum of the recoil electrons in SuperKamiokande. A χ^2 analysis shows that the quality of the rate fits is excellent for two of the field profiles and good for all others with $\chi^2/d.o.f.$ always well below unity. Regarding the fits for the energy spectrum, their quality is better than that for the small mixing angle MSW solution of the solar neutrino problem, at the same level as that for the large mixing angle MSW solution but worse than that for the vacuum oscillations one. The experimental data on the spectrum are however largely uncertain especially in the high energy sector, so that it is too early yet to draw any clear conclusions on the likeliest type of particle physics solution to the solar neutrino problem.

^{*}E-mail: pulido@beta.ist.utl.pt

[†]On leave from National Research Centre Kurchatov Institute, Moscow 123182, Russia. E-mail: akhmedov@gtae2.ist.utl.pt

1 Introduction

More than thirty years after its first recognition [1], the solar neutrino problem has become well established on the grounds of theoretical [2]-[10] versus experimental developments [11]-[14]. The neutrino oscillation solutions to the anomaly, both matter [15] and vacuum oscillations [16], have received a great deal of attention [17]-[23] and became the most popular ones. On the other hand, the solution based on the resonance spin flavour precession (RSFP) mechanism, proposed in 1988 [24], involves the simultaneous flip of both neutrino chirality and flavour [25]. It has been much less thoroughly investigated, in particular concerning its parameter range predictions [26] and the quality of the fits involved [27]. One of the reasons for this comparative lack of popularity may be the large order of magnitude of the neutrino magnetic moment required for a significant conversion and our relatively limited knowledge of the solar magnetic field. It should however be noted that models for a large neutrino magnetic moment not conflicting with the smallness of neutrino mass already exist [28], and there are solar model indications favouring a field as large as 3×10^5 G around the bottom of the convective zone [29]. As shall be seen, the required neutrino magnetic moment is, on the other hand, not inconsistent with astrophysical limits [30], especially taking into account the inherent uncertainties of the analyses.

One of the main motivations for investigating the RSFP mechanism is that neutrinos provide a unique probe for the interior solar magnetic field, if they have a sizeable magnetic moment. In fact, previous analyses [26], [31]-[33] favour solar magnetic fields rising along a relatively short distance (a factor of at least 6-7 over a 7-9% fraction of the solar radius at the most). This rise may be very sharp and even discontinuous profiles are allowed by the data. This appears as a natural consequence of the strong suppression for the intermediate energy neutrinos (^7Be and CNO fluxes) together with the almost no suppression for the low energy pp ones. Solar physics arguments suggest that such a sharp rise, if it exists, must lie around the upper layers of the radiative zone and the bottom of the convective zone. Moreover the moderate suppression of the energetic ^8B neutrinos favours a gradual decrease of the field along the convective zone, with a larger slope at a greater depth.

In this paper we perform an investigation of the RSFP scenario for seven different magnetic field profiles all obeying the general features described above. We start with the numerical integration of the evolution equations for two neutrino flavours, from which we obtain the survival probability as a function of energy. This is used to obtain the event rate in each of the three types of experiments (Gallium, Chlorine and SuperKamiokande). The rates thus obtained are then confronted with the experimental ones [11]-[14]. We let the parameters Δm_{21}^2 (mass square difference between neutrino flavours) and B_0 (value of the field at the peak) run over their "plausible" ranges, namely $4 \times 10^{-9} \text{ eV}^2 \lesssim \Delta m_{21}^2 \lesssim 20 \times 10^{-9} \text{ eV}^2$ and $3 \times 10^4 \text{ G} \lesssim B_0 \lesssim 3 \times 10^5 \text{ G}$. These ranges are "plausible" in the sense that they are dictated by consistency with the RSFP scenario. The first is required by the location of neutrino resonances as a function of energy, so that the most strongly suppressed neutrinos have their resonance around the strongest magnetic field, and the second range by the solar

physics requirement of keeping B_0 not greater than 3×10^5 G at the bottom of the convective zone but large enough to produce significant conversion. For each magnetic field profile we select those intervals in which the theoretical ratios approach their experimental values, and perform a χ^2 analysis in order to determine the local minima and the best fit. We thus get impressively small values of $\chi^2/d.o.f.$, in the range $(3 - 5) \times 10^{-2}$ at the best fit in three of the profiles, two of which are remarkably stable against variations of the parameters Δm_{21}^2 and B_0 . We also compare the theoretical prediction for the recoil electron energy spectrum in SuperKamiokande in each best fit case with the experimental result.

The paper is organized as follows: in section 2 we present the magnetic field profiles to be investigated and the survival probabilities obtained from them upon integration of the evolution equation. In section 3 we calculate the ratios of the event rates predicted in the RSFP scenario to the standard solar model (SSM) event rate in each experiment and analyse their dependence on B_0 and Δm_{21}^2 . Next we describe our χ^2 analysis for the rates and identify the local and absolute minima in each field profile in terms of these parameters. The χ^2 analysis for the electron recoil spectra in SuperKamiokande ends this section. Finally in section 4 we present our summary and overview.

2 Magnetic Field Profiles and Survival Probabilities

In this section we will present the magnetic field profiles to be used throughout, all satisfying the general features explained in the introduction, with a sudden rise around the bottom of the convective zone, at approximately 0.71 of the solar radius, and a smoother decrease up to the surface. Here the field intensity should not exceed a few hundred Gauss. All profiles analysed are displayed in figs. 1 and 2. The first two are simple triangle profiles, with the field intensity rising linearly from zero at fraction $x = x_R$ of the solar radius, reaching a peak at $x = x_C$ and decreasing linearly to zero at the solar surface [31]

$$B = 0 \quad , \quad x < x_R \quad (1)$$

$$B = B_0 \frac{x - x_R}{x_C - x_R} \quad , \quad x_R \leq x \leq x_C \quad (2)$$

$$B = B_0 \left[1 - \frac{x - x_C}{1 - x_C} \right] \quad , \quad x_C \leq x \leq 1 \quad (3)$$

with units in Gauss. We study this class of profiles in two cases shown in fig. 1: profile 1, $x_R = 0.70$, $x_C = 0.85$ (equilateral triangle) and profile 2, $x_R = 0.65$, $x_C = 0.80$ [‡].

Next we consider a slightly larger upgoing slope and a quadratic like decrease up to the surface. This is profile 3 with $x_R = 0.65$, $x_C = 0.75$ (fig. 1)

$$B = 0 \quad , \quad x < x_R \quad (4)$$

[‡]A slight variant of this second profile with a vanishing field for $x \geq 0.95$ was used in ref. [27].

$$B = B_0 \frac{x - x_R}{x_C - x_R}, \quad x_R \leq x \leq x_C \quad (5)$$

$$B = B_0 \left[1 - \left(\frac{x - 0.7}{0.3} \right)^2 \right], \quad x_C < x \leq 1. \quad (6)$$

The two cases with an infinite slope at $x = x_R$ are considered next. The first is profile 4 with the same quadratic like decrease from $x \geq x_R$ up to the surface [31] (fig. 1)

$$B = 0 \quad , \quad x < x_R \quad (7)$$

$$B = B_0 \left[1 - \left(\frac{x - 0.7}{0.3} \right)^2 \right], \quad x \geq x_R, \quad (8)$$

with $x_R = 0.71$ and the second is profile 5 with a reversed shape slope: a strong decrease at first, which then becomes quite moderate on approaching the surface [32, 33] (fig. 2)

$$B = 0 \quad , \quad x < x_R \quad (9)$$

$$B = \frac{B_0}{\cosh 30(x - x_R)}, \quad x \geq x_R \quad (10)$$

with $x_R = 0.71$. Profile 6 is a modification of the previous one with a large finite positive slope across the bottom of the convective zone [26] (fig. 2)

$$B = 2.16 \times 10^3 \quad , \quad x \leq 0.7105 \quad (11)$$

$$B = B_1 \left[1 - \left(\frac{x - 0.75}{0.04} \right)^2 \right], \quad 0.7105 < x < 0.7483 \quad (12)$$

$$B = \frac{B_0}{\cosh 30(x - 0.7483)}, \quad 0.7483 \leq x \leq 1 \quad (13)$$

with $B_0 = 0.998B_1$. The last case considered is profile 7, similar to the previous one but with a linear decrease towards the surface [26] (fig. 2)

$$B = 2.16 \times 10^3 \quad , \quad x \leq 0.7105 \quad (14)$$

$$B = B_0 \left[1 - \left(\frac{x - 0.75}{0.04} \right)^2 \right], \quad 0.7105 < x < 0.7483 \quad (15)$$

$$B = 1.1494B_0[1 - 3.4412(x - 0.71)], \quad 0.7483 \leq x \leq 1. \quad (16)$$

The reasons to select these classes of solar field profiles are twofold: first to investigate previously proposed cases in the light of the most recent experimental data and second to explore those profiles which provide the best and most stable fits against variations of Δm_{21}^2 and B_0 . While, as will be seen, profile 3 provides the best fit of all, this is only marginally better than the fits corresponding to profiles 5 and 6 which are on the other hand much more stable, clearly favouring a specific class of field shape.

We consider the neutrino propagation equation through solar matter which for the two generation Majorana case and zero vacuum mixing angle reads [34, 35]

$$i \frac{d}{dt} \begin{pmatrix} \nu_{eL} \\ \bar{\nu}_{\mu R} \end{pmatrix} = \begin{pmatrix} V_e & \mu_\nu B \\ \mu_\nu B & \frac{\Delta m_{21}^2}{2E} + \bar{V}_\mu \end{pmatrix} \begin{pmatrix} \nu_{eL} \\ \bar{\nu}_{\mu R} \end{pmatrix}. \quad (17)$$

Here V_e and \bar{V}_μ are the matter induced potentials for electron neutrinos and muon antineutrinos respectively, and μ_ν is the neutrino transition magnetic moment.

For definiteness we consider $\nu_{eL} \rightarrow \bar{\nu}_{\mu R}$ transitions but all our results apply to $\nu_{eL} \rightarrow \bar{\nu}_{\tau R}$ transitions as well. We then proceed with the integration of this system of equations using the solar density and neutrino fluxes [36], thus obtaining the survival and conversion probabilities of left handed electron neutrinos. In our numerical calculations we use $\mu_\nu = 10^{-11} \mu_B$. Since the neutrino magnetic moment enters into the evolution equation only in the combination $\mu_\nu B$, the results would also apply to any other value of μ_ν provided that the solar magnetic field strength is rescaled accordingly. For each magnetic field profile the survival probability is given in figs. 3 and 4 for the values of Δm_{21}^2 and B_0 corresponding to the respective best fit. We note the almost total survival of low energy neutrinos, the strong suppression of intermediate energy ones and the moderate suppression of the most energetic ^8B ones. The high energy limit is, in the RSFP case, close to 1/2, as confirmed by these figures, a different situation from MSW where this limit is close to unity. This fact leads in general to better fits of the rates in the case of the RSFP mechanism than in the MSW one. This is because in the case of the MSW mechanism one has to choose very carefully the value of Δm_{21}^2 in order to achieve a factor of $\sim 1/2$ reduction of the high energy portion of ^8B neutrinos, whereas this comes out automatically in the case of the RSFP mechanism.

The next step is to insert the survival probability into the expression for the event rate in each experiment and take the ratio to the SSM event rate. The event rate of the gallium experiments in the framework of the RSFP scenario is calculated as

$$\bar{R}_{Ga} = \sum_i R_{Ga,i} \frac{\bar{R}_{Ga,i}}{R_{Ga,i}} \quad (18)$$

where the sum extends over the relevant neutrino fluxes, ($i = pp, pep, ^7\text{Be}, ^8\text{B}, ^{13}\text{N}, ^{15}\text{O}$). The quantities $\bar{R}_{Ga,i}$ denote the partial event rate for flux i , as predicted by the RSFP model, where, except for $i = ^7\text{Be}, pep$ we have

$$\bar{R}_{Ga,i} = \int_{E_{min}}^{E_{imax}} \sigma_{Ga}(E) P(E) f_i(E) dE. \quad (19)$$

Here $f_i(E)$ represents the i -th flux from ref. [36], and the integral is taken from the experimental threshold $E_{min} = E_{th} = 0.236$ MeV for the pp , ^{15}O , ^{13}N and ^8B cases. For $i = ^7\text{Be}, pep$, the quantities $\bar{R}_{Ga,i}$ are just reduced to the survival probability at the corresponding energy. The quantities $R_{Ga,i}$ are on the other hand the corresponding SSM predictions for

the partial rates [9] obtained from (19) with $P = 1$ (see also table I). The RSFP predicted ratio of the rates for the Gallium experiment is finally

$$r_{Ga} = \frac{\bar{R}_{Ga}}{R_{Ga}} \quad (20)$$

where R_{Ga} is the SSM total rate for the gallium experiment, $R_{Ga} = \sum_i R_{Ga,i}$.

Source	Flux ($10^{10} cm^{-2} s^{-1}$)	Ga (SNU)	Cl (SNU)
pp	5.94	69.6	0.0
pep	1.39×10^{-2}	2.8	0.2
hep	2.1×10^{-7}	0.0	0.0
^7Be	4.8×10^{-1}	34.4	1.15
^8B	5.15×10^{-4}	12.4	5.9
^{13}N	6.05×10^{-2}	3.7	0.1
^{15}O	5.32×10^{-2}	6.0	0.4
^{17}F	6.33×10^{-4}	0.1	0.0
Total		129 ± 8	7.7 ± 1.2 1.0

Table I - Fluxes and partial rates (R_{ji} coefficients in the main text) as predicted by the solar standard model [9].

In order to obtain r_{Cl} this procedure is repeated for the chlorine experiment with the obvious omission of pp neutrinos and the truncation of the other continuous fluxes below $E_{th} = 0.814$ MeV, the energy threshold in the Cl experiment. The SSM rates $R_{Cl,i}$ are also listed in table I. Regarding SuperKamiokande only one neutrino flux is present, namely ^8B [§], and we have for the RSFP predicted ratio

$$\bar{R}_{SK} = \frac{\int_{E_{min}}^{E_{max}} f_{8B}(E) \int_{T_{min}}^{T_{max}} [P(E) \frac{d^2\sigma_W}{dTdE} + [1 - P(E)] \frac{d^2\sigma_{\bar{W}}}{dTdE}] dT dE}{\int_{E_{min}}^{E_{max}} f_{8B}(E) \int_{T_{min}}^{T_{max}} \frac{d^2\sigma_W}{dTdE} dT dE}. \quad (21)$$

Here T is the electron recoil energy, $T_{min} = E_{eth} - m_e$ with $E_{eth} = 5.5$ MeV [14]

$$T_{max} = \frac{2E^2}{2E + m_e} \quad (22)$$

and the integration limits for the neutrino energy are respectively,

$$E_{min} = \frac{T_{min} + \sqrt{T_{min}^2 + 2m_e T_{min}}}{2} \quad (23)$$

[§]The contribution of a small flux of *hep* neutrinos is completely negligible in the total rates but may be of some importance for the high energy part of the recoil electron spectrum in SuperKamiokande. We shall discuss this point in more detail in section 4.

and $E_{max} = 15$ MeV. The weak interaction differential cross section for $\nu_e e$ scattering is given by

$$\frac{d^2\sigma_W}{dTdE} = \frac{G_F^2}{2\pi m_e} [(g_V + g_A)^2 + (g_V - g_A)^2 \left(1 - \frac{T}{E}\right)^2 - (g_V^2 - g_A^2) \frac{m_e T}{E^2}] \quad (24)$$

with $g_V = \frac{1}{2} + 2\sin^2\theta_W$, $g_A = \frac{1}{2}$. The cross section for $\bar{\nu}_\mu e$ and $\bar{\nu}_\tau e$ scattering is on the other hand

$$\frac{d^2\sigma_{\bar{W}}}{dTdE} = \frac{G_F^2}{2\pi m_e} [(g_V - g_A)^2 + (g_V + g_A)^2 \left(1 - \frac{T}{E}\right)^2 - (g_V^2 - g_A^2) \frac{m_e T}{E^2}] \quad (25)$$

with $g_V = -\frac{1}{2} + 2\sin^2\theta_W$, $g_A = -\frac{1}{2}$. The contribution of the neutrino electromagnetic cross section to eq. (21) is negligible, typically 3 orders of magnitude lower than the weak cross section and will be omitted. We do not include the electron energy resolution function of the detector as its effect on the total rate is negligible; we will, however, include it in the calculation of the recoil electron spectrum. We calculate the ratios $r_{Ga}, r_{Cl}, \bar{R}_{SK}$ in the parameter ranges $\Delta m_{21}^2 = (4 - 20) \times 10^{-9}$ eV² and $B_0 = (3 - 30) \times 10^4$ G for all seven magnetic field profiles presented above and identify in each case those intervals in which all three ratios simultaneously approach their experimental values (table II). We then perform for each interval a χ^2 analysis in order to evaluate the quality of the fit.

Experiment	Data	Theory	Data/Theory	Reference
Homestake	$2.56 \pm 0.16 \pm 0.15$	$7.7 \pm_{1.0}^{1.2}$	0.33 ± 0.03	[11]
Gallex	$76.4 \pm 6.3 \pm_{4.9}^{4.5}$	$129 \pm_6^8$	0.59 ± 0.06	[13]
SAGE	$69.9 \pm_{7.7 \pm 4.1}^{8.0 \pm 3.9}$	$129 \pm_6^8$	0.54 ± 0.06	[12]
SuperKamiokande	$2.44 \pm 0.05 \pm_{0.06}^{0.09}$	$5.15 \pm_{0.7}^{1.0}$	0.474 ± 0.020	[14]

Table II - Data from the four solar neutrino experiments. Units are SNU for the first three experiments and in $\text{cm}^{-2}\text{s}^{-1}$ for SuperKamiokande. For the Gallium experiments we have used the combined result 72.3 ± 5.6 SNU.

3 Analysis of the data

3.1 Description of χ^2 analysis

We follow in this subsection the procedure outlined in ref. [37] adapted to the RSFP mechanism and the present experimental situation [11]-[14]. We start with the definition of the χ^2 function

$$\chi^2 = \sum_{j_1, j_2=1}^3 (\bar{R}_{j_1} - R_{j_1}^{exp}) \left[\sigma^2(tot) \right]_{j_1 j_2}^{-1} (\bar{R}_{j_2} - R_{j_2}^{exp}). \quad (26)$$

In this expression the indices j_1, j_2 run over the three types of experiments: Ga, Cl and SuperKamiokande respectively. The quantities \bar{R} denote the theoretical (RSFP) event rates defined in eqs. (18), (19) for Ga and Cl experiments, and in (20) for the SuperKamiokande one and the quantities R^{exp} denote the experimental ones given in table II. They are expressed in SNU for Ga, Cl and in terms of the ratio data/SSM for SuperKamiokande. For the Gallium case we use the combined value from SAGE and Gallex, $R_{Ga}^{exp} = 72.3 \pm 5.6$ SNU. The matrix $\sigma_{j_1 j_2}^2(tot)$ is the total error matrix given by

$$\sigma_{j_1 j_2}^2(tot) = \sigma_{j_1 j_2}^2(exp) + \sigma_{j_1 j_2}^2(th). \quad (27)$$

The experimental error matrix is given in terms of σ_j^{exp} , the experimental errors shown in table I,

$$\sigma_{j_1 j_2}^2(exp) = \delta_{j_1 j_2} \sigma_{j_1}^{exp} \sigma_{j_2}^{exp} \quad (28)$$

so that

$$\sigma_{j_1 j_2}^2(exp) = \begin{pmatrix} 31.36 & 0 & 0 \\ 0 & 0.0481 & 0 \\ 0 & 0 & 0.0004 \end{pmatrix}. \quad (29)$$

The theoretical error matrix in eq. (27) is the sum of the cross section contribution containing the uncertainties in the cross sections with the astrophysical contribution involving the uncertainties in the astrophysical parameters

$$\sigma_{j_1 j_2}^2(th) = \sigma_{j_1 j_2}^2(cs) + \sigma_{j_1 j_2}^2(ap). \quad (30)$$

The uncertainties in the detector cross sections, expressed in the form $\Delta \ln C_{ij}$, entering the cross section error matrix, are assumed uncorrelated and were taken from ref. [4]. They give rise to the following diagonal matrix

$$\sigma_{j_1 j_2}^2(cs) = \delta_{j_1 j_2} \sum_{i=1}^6 \bar{R}_{ij_1}^2 (\Delta \ln C_{ij_1})^2. \quad (31)$$

where the index i runs over all relevant fluxes, $i = pp, pep, {}^7\text{Be}, {}^8\text{B}, {}^{13}\text{N}, {}^{15}\text{O}$. Model dependence appears in this matrix through the \bar{R}'_{ij} s.

The astrophysical error matrix is finally

$$\sigma_{j_1 j_2}^2(ap) = \sum_{i_1, i_2=1}^6 \bar{R}_{j_1 i_1} \bar{R}_{j_2 i_2} \sum_{k=1}^9 \alpha_{i_1 k} \alpha_{i_2 k} (\Delta \ln X_k)^2 \quad (32)$$

In this expression index k extends over the nine astrophysical parameters $k = S_{11}, S_{33}, S_{34}, S_{1,14}, S_{17}, Lum, Z/X, Age, Opac$, the α matrix denotes the logarithmic derivatives of the six fluxes considered with respect to these parameters, $\alpha_{ik} = \partial \ln f_i / \partial \ln X_k$ and the rest of the notation is self clear. The (6×9) matrix

$$\alpha_{ik} \Delta \ln X_k \quad (33)$$

which appears in equation (32) was calculated using the data from [36]. We now have all the necessary elements to calculate χ^2 for each magnetic field profile.

3.2 Fits of the rates and their quality

In this subsection we will investigate the local minima of χ^2 for all studied solar field profiles, identifying in each profile the lowest minimum in terms of B_0 (peak field value) and Δm_{21}^2 . As discussed in the introduction we analyze the intervals $B_0 = (3 - 30) \times 10^4$ G and $\Delta m_{21}^2 = (4 - 20) \times 10^{-9}$ eV², the first interval dictated by the requirement of significant neutrino conversion (lower bound) and solar physics arguments [29] (upper bound) and the second interval dictated by the resonance locations of the several neutrino fluxes. In fitting the rates we have three types of experiments (Ga, Cl, SuperKamiokande) and two parameters: $\Delta m_{21}^2, \mu_\nu B_0$ for a given magnetic field profile. Hence the number of degrees of freedom is one. We search for values of χ^2 smaller than or of order unity and discuss the profiles in the same order as in section 2. Starting therefore with profile 1 (equilateral triangle), eqs. (1)-(3), we observe two local minima (fig. 5), one at $B_0 \simeq 1.68 \times 10^5$ G and the other at $B_0 \simeq 2.71 \times 10^5$ G, both with $\Delta m_{21}^2 \simeq 8 \times 10^{-9}$ eV². The first is an absolute minimum with $\chi^2_{min} = 0.085$ and for the second, $\chi^2_{min} = 0.137$. While such values of χ^2 (especially the first one) are remarkably low, the stability of both fits against small parameter variations is rather poor: a change of 3 kG in the value of B_0 implies a change in χ^2 by a factor of order 30.

The second profile is the triangle field, eqs (1)-(3), in which we identified three local minima (fig. 6): the best fit ($\chi^2_{min} = 0.10$) corresponds to $B_0 \simeq 1.23 \times 10^5$ G, $\Delta m_{21}^2 \simeq 1.20 \times 10^{-8}$ eV², the second best ($\chi^2_{min} = 0.284$) to $B_0 \simeq 1.98 \times 10^5$ G, $\Delta m_{21}^2 \simeq 1.20 \times 10^{-8}$ eV² and the third ($\chi^2_{min} = 0.553$) to $B_0 \simeq 2.85 \times 10^5$ G, $\Delta m_{21}^2 \simeq 1.25 \times 10^{-8}$ eV². These minima are displayed in fig. 6 and it is seen that their stability is better than the previous cases: a change of 3 kG implies a change in χ^2 by a factor of 3-4.

Next we examine profile 3, eqs. (4)-(6): there are two local minima of χ^2 both corresponding to $\Delta m_{21}^2 \simeq 1.2 \times 10^{-8}$ eV² (fig. 7), the first one at $B_0 = 9.54 \times 10^4$ G with an impressively low χ^2 ($\chi^2_{min} = 0.036$) and the second one at $B_0 \simeq 1.72 \times 10^5$ G ($\chi^2_{min} = 0.11$). We note the extreme instability of the first, where the same change of 3 kG in B_0 leads to a change in χ^2 by a factor of 50, while for the second the corresponding factor is of order 30.

Profile 4, eqs. (7), (8), shows two local minima of χ^2 (fig. 8): $\chi^2_{min} = 0.68$ for $\Delta m_{21}^2 \simeq 1.2 \times 10^{-8}$ eV², $B_0 = 9.0 \times 10^4$ G and $\chi^2_{min} = 0.59$ for $\Delta m_{21}^2 \simeq 1.6 \times 10^{-8}$ eV², $B_0 = 1.7 \times 10^5$ G. These fits are poorer than the previous ones and in addition they are also quite unstable: a factor of at least 10 increase in χ^2 for a 3 kG change in the field at the peak. Of all cases examined, such a profile appears to be the least favoured by the data. If in this case we choose a power greater than 2 in eq. (8), the results become even worse as the SuperKamiokande and Chlorine rates become too close to each other.

The essential difference between profile 5, eqs. (9), (10), and the previous one is the shape of the decrease along the convective zone. This is enough to ensure a totally different quality of the fit. In fact we observe only one very stable minimum in the whole B_0 range with an extremely low χ^2 (fig. 9): $\chi^2_{min} = 0.054$ for $\Delta m_{21}^2 \simeq 2.1 \times 10^{-8}$ eV², $B_0 \simeq 1.45 \times 10^5$

G. The stability of this minimum is in sharp contrast with previous cases, as a change of 15 kG in the peak field implies a change in χ^2 by a factor of 2 at the most. An obvious conclusion from the comparison with the previous case is that the data prefers a profile with an upward facing concavity relative to a downward one along the convective zone. This is to be expected, since the low energy sector of the ^8B neutrinos necessarily undergoes a strong suppression as the corresponding energy is in the intermediate range, where suppression is maximal. Hence in order to ensure a moderate suppression for the whole ^8B flux, its high energy part must be suppressed to a much lesser extent implying a strong decrease of the field as from the start of the convective zone. It should be noted that such profiles are also expected to provide better fits of the high energy part of the recoil electron spectrum in SuperKamiokande, as they lead to a weaker suppression of the high energy part of the solar neutrino spectrum (see next subsection).

Profile 6, eqs. (11)-(13), also shows a remarkably good and stable fit. Its general shape is roughly the same as the previous one, the only difference being a finite upward slope at the bottom of the convective zone. The best fit ($\chi^2_{\min} = 0.047$) is for $\Delta m_{21}^2 \simeq 1.60 \times 10^{-8} \text{ eV}^2$, $B_0 \simeq 9.6 \times 10^4 \text{ G}$ (see fig. 10). It is also seen that a change of 11 kG implies a change by a factor of 5 in χ^2 . A second, poorer fit, also shows up in this case: $\chi^2_{\min} = 0.65$ for $\Delta m_{21}^2 \simeq 1.3 \times 10^{-8} \text{ eV}^2$, $B_0 \simeq 2.63 \times 10^5 \text{ G}$.

Finally we examined profile 7. There are four local minima of χ^2 in this case, all providing fits that are poor and relatively unstable in comparison with the previous ones. We have (see fig. 11) : $\chi^2_{\min} = 0.84$ for $\Delta m_{21}^2 \simeq 1.1 \times 10^{-8} \text{ eV}^2$, $B_0 \simeq 1.26 \times 10^5 \text{ G}$, $\chi^2_{\min} = 0.53$ for $\Delta m_{21}^2 \simeq 1.2 \times 10^{-8} \text{ eV}^2$, $B_0 \simeq 1.66 \times 10^5 \text{ G}$, $\chi^2_{\min} = 0.71$ for $\Delta m_{21}^2 \simeq 1.4 \times 10^{-8} \text{ eV}^2$, $B_0 \simeq 2.3 \times 10^5 \text{ G}$, $\chi^2_{\min} = 0.875$ for $\Delta m_{21}^2 \simeq 1.2 \times 10^{-8} \text{ eV}^2$, $B_0 \simeq 2.7 \times 10^5 \text{ G}$. A change of 3 kG in the central value of B_0 implies an increase of χ^2 by a factor of at least 6. This profile is therefore manifestly disfavoured relative to profile 6. It is worth noting that the difference between the two lies only in the shape of the downward slope along the convective zone.

3.3 Fits of the recoil spectra and their quality

In this subsection we calculate the spectrum of recoil electrons in SuperKamiokande for each of the magnetic field profiles 1-7. We take in each case the values of $(\Delta m_{21}^2, B_0)$ that correspond to the best fit of the rates as calculated in the previous subsection and evaluate the corresponding χ^2 of the spectrum. We also determine for the cases whose fits and stability are the best (profiles 5 and 6) the minimum χ^2 and corresponding $(\Delta m_{21}^2, B_0)$. The starting point is the ratio of the SuperKamiokande event rate to the one predicted by the SSM evaluated for the 18 energy bins ($j = 1, \dots, 18$)

$$R_j = \frac{\int_{E_j}^{E_{j+1}} dE_e \int_0^\infty dE'_e f(E_e, E'_e) \int_{E_{\min}(E'_e)}^\infty dE f_{\text{SB}}(E) \left(P(E) \frac{d^2\sigma_W}{dTdE} + [1 - P(E)] \frac{d^2\sigma_{\bar{W}}}{dTdE} \right)}{\int_{E_j}^{E_{j+1}} dE_e \int_0^\infty dE'_e f(E_e, E'_e) \int_{E_{\min}(E'_e)}^\infty dE f_{\text{SB}}(E) \frac{d^2\sigma_W}{dTdE}} \quad (34)$$

where, $f(E_e, E'_e)$ is the energy resolution function which can be found in [38], $E_e = T + m_e$, and the rest of the notation was defined in section 2. In fig. 12 we plot R_j corresponding to profiles 5 and 6 superimposed on data set II.

As far as the χ^2 analysis is concerned there is only one flux now and the values to be fitted are the 18 data points given by the SuperKamiokande collaboration (set I [39] and set II [40] with 708 days and 825 days respectively of data taking). Hence the definition of χ^2 is now

$$\chi^2 = \sum_{j_1, j_2=1}^{18} (\bar{R}_{j_1} - R_{j_2}^{exp}) [\sigma^2(tot)]_{j_1 j_2}^{-1} (\bar{R}_{j_2} - R_{j_2}^{exp}). \quad (35)$$

Here the quantities $\bar{R}_{j_1}, \bar{R}_{j_2}$ denote the vector elements given by (34). Since only one neutrino flux is considered here, namely ${}^8\text{B}$, in calculating $\sigma^2(ap)$ the matrix within the second summation in equation (32) has now been reduced to its column vector corresponding to $i_1 = i_2 = 4 = {}^8\text{B}$. We thus have

$$\sigma_{j_1 j_2}^2(ap) = \bar{R}_{j_1} \bar{R}_{j_2} \sum_{k=1}^9 \alpha_{4k}^2 (\Delta \ln X_k)^2 \quad (36)$$

where $j_1, j_2 = 1, \dots, 18$. The matrix elements of $\sigma(exp)$ (28) are directly read from [39] and [40], the matrix $\sigma(cs)$ can be taken to be zero since the uncertainties in the cross sections of νe scattering are negligible.

Evaluating χ^2 for the spectrum using the values of $(\Delta m_{21}^2, B_0)$ that correspond to the best fit of the rates, we find the results shown in table III for each field profile and data set. It is worth noting that the profiles that generate the best and most stable fits (5 and 6) for the rates are also those that lead to the lowest χ^2 for the spectrum. We have calculated for these two the minimum χ^2 (for data set II) and found for case 5 a minimum at $(3.2 \times 10^{-8} \text{ eV}^2, 1.14 \times 10^5 G)$ ($\chi_{spmin}^2 = 23.235$) to be compared with (see section 3.2) $(2.1 \times 10^{-8} \text{ eV}^2, 1.45 \times 10^5 G)$ for the rates. For case 6 (data set II) we found a minimum at $(2.4 \times 10^{-8} \text{ eV}^2, 1.12 \times 10^5 G)$ ($\chi_{spmin}^2 = 23.236$) to be compared with (see section 3.2) $(1.6 \times 10^{-8} \text{ eV}^2, 9.6 \times 10^4 G)$ for the rates. The stability of these fits should be stressed, as in fact the change in the value of χ^2 between the two minima (for the rates and spectrum) in each of the two profiles only affects the third digit of χ^2 . For this reason we do not include the χ_{sp}^2 plots in the paper.

We note finally that although the fits for data set II are slightly worse than those for data set I, the differences in χ^2 are only marginal. Furthermore, one must keep in mind that the large uncertainties still present in the high energy ($E_e > 13 \text{ MeV}$) part of the spectrum and the differences in the central data points for sets I and II make it difficult to draw any definitive conclusions about the particle-physics solution of the solar neutrino problem favoured by the recoil electron spectrum.

Profile	$\chi_{sp}^2(I)$	$\chi_{sp}^2(II)$
1	22.5	24.8
2	21.9	23.9
3	22.5	24.8
4	25.9	29.5
5	21.6	23.5
6	21.7	23.6
7	22.3	24.5

Table III - The values of χ^2 (16 d.o.f.) for the recoil electron spectrum in SuperKamiokande evaluated for $\Delta m_{21}^2, B_0$ which correspond to the best fits of the rates. Data sets (I) and (II) are given in refs. [39], [40] and profiles 1-7 are shown in figs. 1 and 2. Cases 5 and 6, besides providing the lowest χ_{sp}^2 's, also give the lowest χ^2 's for the rates and, interestingly enough, the most stable fits of all.

4 Summary and Discussion

We have examined the status of the RSFP solution to the solar neutrino problem in the light of the most recent experimental data on total rates and energy spectrum and the standard solar model of BP98 [9]. There is independent, although scarce, input information from solar physics on the solar magnetic field [29] suggesting a field that is largest around the bottom of the convective zone with a peak up to 3×10^5 G in that region. So at the start of any RSFP analysis one cannot consider the field profile as entirely free. On the other hand previous studies indicate that the common suppression of intermediate energy neutrinos and the almost total survival of low energy ones must lead, if neutrinos have a magnetic moment, to a profile rising sharply over a relatively short distance along the solar radius, decreasing then smoothly towards the surface. Using this input information we investigated a general class of profiles with the above characteristics and calculated for each of them the values of $\Delta m_{21}^2, B_0$ which provide the best fits for the total rates.

The shape of the survival probability as a function of neutrino energy is obviously determinant for the quality of these fits. One important general feature is that the limit of this probability as the energy increases is close to 1/2 in the case of RSFP, whereas in the case of MSW it is close to unity. Hence the important contribution of the ^8B neutrinos, which survive up to a factor of almost 1/2 and whose energy spread is large, is naturally much better fitted in RSFP than in MSW. Thus the fact that the values of χ_{min}^2 for the rates best fits range from 0.036 to 0.59 for 1 d.o.f. (profiles 3 and 4 respectively), to be compared with 1.7 (SMA solution) and 4.3 (LMA and vacuum oscillation solutions) [18], is not surprising ¶.

¶It should be noted that smaller values of χ_{min}^2 for the MSW solutions were obtained in [20]: $\chi_{min}^2 = 0.44$ for the SMA and $\chi_{min}^2 = 2.7$ for the LMA solution.

The investigation performed for the rates fits has taught us that, besides a fast rise across the bottom of the convective zone, the magnitude of the field should decrease faster past this bottom and then slower on approaching the solar surface. In other words, the profile must show an upward facing concavity. To this end it suffices to compare the fits of profiles 4 with 5 on one hand and the fits of profiles 6 with 7 on the other. The very low χ^2 obtained for profile 3 (0.036), with the reverse concavity, is extremely unstable as compared to the "best" cases 5 and 6. This fact may be easily understood if one notes that the low energy sector of the ^8B neutrinos has to be highly depleted because their energies are close to those of ^7Be , CNO and *pep* neutrinos which must be strongly suppressed by RSFP in order to fit the data. On the other hand, the overall suppression of ^8B neutrinos is just moderate. So the solar field must ensure a small suppression of their high energy sector. This is achieved if the field becomes much weaker soon after the intermediate resonance densities. Hence an upward facing concavity of the field profile along the convective zone appears to be favoured.

We have also calculated the recoil electron energy spectra in SuperKamiokande and performed the corresponding fits for the same class of field profiles. We found for all of them except one (profile 4) the correct sign slope against the recoil electron energy. Regarding the high energy bins, the central data points show the excess of the observed number of events compared with the theoretical predictions, but it should be stressed that the uncertainties are much larger in this sector. Hence the general quality of the fits for the spectra is also encouraging. We found, with 16 d. o. f., $(\chi^2_{sp})_{min}$ ranging from 21.6 to 25.9 (data set I [39], profiles 5 and 4 respectively) and 23.4 to 29.5 (data set II [40], also profiles 5 and 4 respectively). All minima are quite shallow. These values are to be compared with 25.0 [40] (24.1 [20]) for the SMA solution, 23.5 [20] for the LMA solution and 17.4 [40] for the vacuum oscillations solution. Future data on the SuperKamiokande energy spectrum are thus eagerly awaited, especially regarding the improvement in accuracy of its upper and lower ranges. In fact, determining whether the spectrum really rises with energy for $E_e > 13$ MeV or else the apparent rise is just a statistical fluctuation or an instrumental effect will be essential to discriminate between various solutions of the solar neutrino problem. As it stands, no theoretical model (oscillations or RSFP) is able to provide a very good fit.

It should be noted that reasonably good fits of the spectrum can be achieved in all scenarios if one treats the poorly known flux of *hep* neutrinos, which constitutes the highest energy component of the solar neutrino spectrum, as a free parameter [41, 19, 20, 40]. We did not perform such an analysis because the latest SuperKamiokande data shows the decreased excess of high energy events [40] and it may therefore be advisable to wait until more accurate data has been obtained.

We have used throughout a value of $10^{-11}\mu_B$ for the neutrino magnetic moment. Since the order parameter is the product $\mu_\nu B$ (eq. (17)) and the peak field may be as large as 3×10^5 G, a factor of 2-3 larger than its best fits, the appropriate order of magnitude for μ_ν is in fact $(3 - 5) \times 10^{-12}\mu_B$, a value consistent with most astrophysical bounds [30].

To conclude, the prospects of RSFP as a possible solution to the solar neutrino problem are at present quite encouraging: in fact the fits to the total rates are excellent, far better than in any other scenario [18, 19, 20]. As far as the fits for the recoil electron energy spectrum are concerned, they are in general slightly better than the small mixing angle MSW ones, similar to the large mixing angle MSW ones and worse than vacuum oscillation ones, depending of course on the appropriate choice of the field profile. The improvement in the data on the spectrum, will be essential in helping to ascertain the most realistic theoretical model.

Acknowledgements

The work of one of us (E. A.) work was supported by Fundação para a Ciência e a Tecnologia through the grant PRAXIS XXI/BCC/16414/98 and also in part by the TMR network grant ERBFMRX-CT960090 of the European Union. We are grateful to M. Guzzo and H. Nunokawa for useful correspondence.

References

- [1] R. Davis, D. S. Harmer and K. C. Hoffman, Phys. Rev. Lett. **20**, 1205 (1968).
- [2] S. Turck-Chieze and I. Lopes, Astrophys. J. **408**, 347 (1993).
- [3] S. Turck-Chieze, S. Cahen, M. Casse and C. Doom, Astrophys. J. **335**, 415 (1988).
- [4] J. N. Bahcall and M. H. Pinsonneault, Rev. Mod. Phys. **64** (1992) 885.
- [5] C. R. Profitt, Astrophys. J. **425**, 849 (1994).
- [6] O. Richard *et al.*, Astron. Astrophys. **312** 1000 (1996).
- [7] S. Degl’Innocenti *et al.*, Astron. Astrophys., Suppl. Ser. **123**, 1 (1997).
- [8] J. N. Bahcall and M. H. Pinsonneault, Rev. Mod. Phys. **67**, 781 (1995).
- [9] J. N. Bahcall, S. Basu and M. H. Pinsonneault. Phys. Lett. **433** 1 (1998).
- [10] A. S. Brun, S. Turck-Chieze and P. Morel, astro-ph/9806272, to be published in Astrophys. J. **506** (1998).
- [11] B. T. Cleveland *et al.*, Astrophys. J. **496**, 505 (1998); B. T. Cleveland *et al.*, Nucl. Phys. **B** (Proc. Suppl.) **38**, 47 (1995); R. Davis, Prog. Part. Nucl. Phys. **32**, 13 (1994).

- [12] SAGE Collaboration, V. Gavrin *et al.*, in *Neutrino 98*, Proceedings of the XVIII International Conference on Neutrino Physics and Astrophysics, Takayama, Japan, 4-9 June 1998, edited by Y. Suzuki and Y. Totsuka. To be published in Nucl. Phys. **B** (Proc. Suppl.).
- [13] Gallex Collaboration, P. Anselmann *et al.*, Phys. Lett. **B 342**, 440 (1995); W. Hampel *et al.*, Phys. Lett. **B 388**, 364 (1996).
- [14] SuperKamiokande Collaboration, Y. Suzuki in *Neutrino 98* [12].
- [15] L. Wolfenstein, Phys. Rev. **D 17**, 2369 (1978); **20**, 2634 (1979); S. P. Mikheyev and A. Smirnov, Sov. J. Nucl. Phys. **42**, 913 (1985).
- [16] B. Pontecorvo, Zh. Exp. Theor. Fiz. **53** (1967) 1717; V. Gribov and B. Pontecorvo, Phys. Lett. **28B** (1969) 493; V. Barger, R. J. N. Phillips and K. Whisnant, Phys. Rev. **D24** (1981) 538; S. L. Glashow and L. M. Krauss, Phys. Lett. **B190** (1987) 199; P. I. Krastev and S. T. Petcov, Phys. Rev. **D53** (1996) 1665; E. Calabresu *et al.*, Astropart. Phys. **4** (1995) 159; Z. G. Berezhiani and A. Rossi, Phys. Rev. **D51** (1995) 5229; Phys. Lett. **B367** (1996) 219.
- [17] N. Hata, P. Langacker, Phys. Rev. **D56** (1997) 6107.
- [18] J. N. Bahcall, P. I. Krastev and A. Yu. Smirnov, Phys. Rev. **D 58** 096016 (1998);
- [19] J. N. Bahcall, P. I. Krastev and A. Yu. Smirnov, hep-ph/9905220;
- [20] M.C. Gonzalez-Garcia, P.C. de Holanda, C. Pena-Garay and J.W.F. Valle, FTUV-99-41, hep-ph/9906469.
- [21] S. P. Mikheyev and A. Yu. Smirnov, Phys. Lett. **B429** (1998) 343; V. Berezinsky, G. Fiorentini and M. Lissia, hep-ph/9811352, hep-ph/9904225; V. Barger and K. Whisnant, Phys. Lett. **B456** (1999) 54; Phys. Rev. **D59**, 093007, 1999;
- [22] A. Yu. Smirnov, Invited talk at 18th International Conference on Neutrino Physics and Astrophysics (NEUTRINO 98), Takayama, Japan, 4-9 Jun 1998, hep-ph/9809481.
- [23] V. Berezinsky Talk given at 19th Texas Symposium on Relativistic Astrophysics: Texas in Paris, Paris, France, 14-18 Dec. 1998, hep-ph/9904259
- [24] C. S. Lim and W. J. Marciano, Phys. Rev. **D37**, 1368 (1988); E. Kh. Akhmedov, Sov. J. Nucl. Phys. **48**, 382 (1988); E. Kh. Akhmedov, Phys. Lett. **B 213**, 64 (1988).
- [25] J. Schechter and J. W. F. Valle, Phys. Rev. **D24**(1981) 1883, Erratum-*ibid.* **D25** (1982) 283.
- [26] J. Pulido, Phys. Rev. **D57**, 7108 (1998).

- [27] M. Guzzo and H. Nunokawa, preprint hep-ph/9810408, to be published in *Astrop. Phys.*.
- [28] K.S. Babu and R.N. Mohapatra, *Phys. Rev. Lett.* **63** (1989) 228; *Phys. Rev.* **D42** (1990) 3778; S. M. Barr, E. M. Freire, A. Zee, *Phys. Rev. Lett.* **65**, 2626 (1990).
- [29] E. N. Parker in "The Structure of the Sun", Proc. of the VI Canary Islands School, Ed. Roca Cortes and F. Sanchez, Cambridge University Press 1996 p. 299.
- [30] S. I. Blinnikov, Institute for Theoretical and Experimental Physics Report No. ITEP-88-19 (1988), unpublished; S. I. Blinnikov, V.S. Imshennik, D.K. Nadyozhin, *Sov. Sci. Rev. E Astrophys. Space Sci.* **6**, 185 (1987); G.G. Raffelt, *Phys. Rev. Lett.* **64** (1990) 2856; *Astrophys. J.* **365** (1990) 559; V. Castellani and S. Degl'Innocenti, *Astrophys. J.* **402**, 574 (1993).
- [31] E. Kh. Akhmedov, A. Lanza and S. T. Petcov, *Phys. Lett.* **B 303**, 85 (1993).
- [32] E. Kh. Akhmedov and O.V. Bychuk, *Sov. Phys. JETP* **68** (1989) 250.
- [33] E. Kh. Akhmedov, A. Lanza and S. T. Petcov, *Phys. Lett.* **B 348**, 124 (1995).
- [34] See e. g. J. Pulido, *Phys. Rep.* **211**, 167 (1992).
- [35] E. Kh. Akhmedov, Talk given at 4th International Solar Neutrino Conference, Heidelberg, Germany, 8-11 Apr 1997, hep-ph/9705451.
- [36] J. N. Bahcall's homepage, <http://www.sns.ias.edu/~jnb/>.
- [37] G. L. Fogli and E. Lisi, *Astrop. Phys.* **3**, 185 (1995).
- [38] Super-Kamiokande Collaboration, Y. Fukuda *et al.*, *Phys. Rev. Lett.* **81** (1998) 1158; Erratum-*ibid.* **81** (1998) 4279.
- [39] SuperKamiokande Collaboration, Y. Suzuki, Talk at XVII Int. Workshop on Weak Interactions and Neutrinos, Cape Town, South Africa, Jan 24-30, 1999.
- [40] SuperKamiokande Collaboration, T. Kajita, Talk at *Beyond the Desert'99*, Ringberg Castle, Germany, June 6-12, 1999.
- [41] R. Escribano, J. M. Frere, A. Gevaert and D. Monderen, *Phys. Lett.* **B444** (1998) 397; J. N. Bahcall and P. I. Krastev, *Phys. Lett.* **B436** (1998) 243.

Figure captions

Fig. 1. Solar magnetic fields as functions of the solar coordinate $x = r/R_S$. Field strength is in Gauss. Solid line is profile 1 [eqs. (1) - (3) with $x_R = 0.7, x_C = 0.85$], dotted line is profile 2 [eqs. (1) - (3) with $x_R = 0.65, x_C = 0.8$], dashed line is profile 3 [eqs. (4) - (6)], long-dashed line is profile 4 [eqs. (7), (8)]. For $x > 0.75$ profiles 3 and 4 coincide.

Fig. 2. Profile 5 [solid line, eqs. (9), (10)] profile 6 [dotted line, eqs. (11) - (13)], profile 7 [dashed line, eqs. (14) - (16)]. For $0.71 \leq x \leq 0.75$ profiles 6 and 7 coincide.

Fig. 3. Neutrino survival probabilities for profiles 1 - 4 as functions of neutrino energy for Δm_{21}^2 and B_0 given by their values at the best fit of the rates for each profile. Solid line corresponds to profile 1, dotted line, to profile 2, dashed line, to profile 3, long dashed line, to profile 4.

Fig. 4. Same as fig. 3 for the neutrino survival probabilities for profiles 5 - 7. Solid line corresponds to profile 5, dotted line to profile 6 and dashed line to profile 7.

Fig. 5. Rate fits: values of $\chi^2/d.o.f.$ as functions of the peak value of the field for profile 1 for several values of Δm_{21}^2 . Left: dashed line corresponds to 7×10^{-9} eV², full to 8×10^{-9} eV², dotted to 9×10^{-9} eV². Right: dotted line corresponds to 7×10^{-9} eV², full to 8×10^{-9} eV², dashed to 9×10^{-9} eV². Best fit: $\Delta m_{21}^2 = 8 \times 10^{-9}$ eV², $B_0 = 1.68 \times 10^5$ G, $\chi_{min}^2/d.o.f. = 0.085$.

Fig. 6. Rate fits: $\chi^2/d.o.f.$ as a function of the peak field value for several values of Δm_{21}^2 for profile 2. Top left: dashed 1.15×10^{-8} eV², full 1.2×10^{-8} eV², dotted 1.25×10^{-8} eV². Top right: full 1.3×10^{-8} eV², dotted 1.35×10^{-8} eV², dashed 1.40×10^{-8} eV². Bottom left: dotted 1.15×10^{-8} eV², full 1.20×10^{-8} eV², dashed 1.25×10^{-8} eV². Bottom right: dotted 1.15×10^{-8} eV², dashed 1.20×10^{-8} eV², full 1.25×10^{-8} eV². Best fit: $\Delta m_{21}^2 = 1.20 \times 10^{-8}$ eV², $B_0 = 1.23 \times 10^5$, $\chi_{min}^2/d.o.f. = 0.100$.

Fig. 7. Rate fits: $\chi^2/d.o.f.$ as a function of the peak field (profile 3) for several values of Δm_{21}^2 . Left: dotted 1.1×10^{-8} eV², full 1.2×10^{-8} eV², dashed 1.3×10^{-8} eV². Right: dot-dashed 1.1×10^{-8} eV², full 1.2×10^{-8} eV², dotted 1.3×10^{-8} eV², dashed 1.4×10^{-8} eV². Best fit: $\Delta m_{21}^2 = 1.2 \times 10^{-8}$ eV², $B_0 = 9.54 \times 10^4$ G, $\chi_{min}^2/d.o.f. = 0.036$.

Fig. 8. Rate fits: $\chi^2/d.o.f.$ as a function of the peak field (profile 4) for several values of Δm_{21}^2 . Left: dashed 1.1×10^{-8} eV², full 1.2×10^{-8} eV², dotted 1.3×10^{-8} eV². Right: dashed 1.5×10^{-8} eV², full 1.6×10^{-8} eV², dotted 1.7×10^{-8} eV². Best fit: $\Delta m_{21}^2 = 1.6 \times 10^{-8}$ eV², $B_0 = 1.7 \times 10^5$ G, $\chi_{min}^2/d.o.f. = 0.59$.

Fig. 9. Rate fits: $\chi^2/d.o.f.$ as a function of the peak field for profile 5 for several values of Δm_{21}^2 . Dotted line 1.9×10^{-8} eV², dashed 2.0×10^{-8} eV², full 2.1×10^{-8} eV², dot-dashed 2.2×10^{-8} eV². Best fit: $\Delta m_{21}^2 = 2.1 \times 10^{-8}$ eV², $B_0 = 1.45 \times 10^5$ G, $\chi_{min}^2/d.o.f. = 0.0547$.

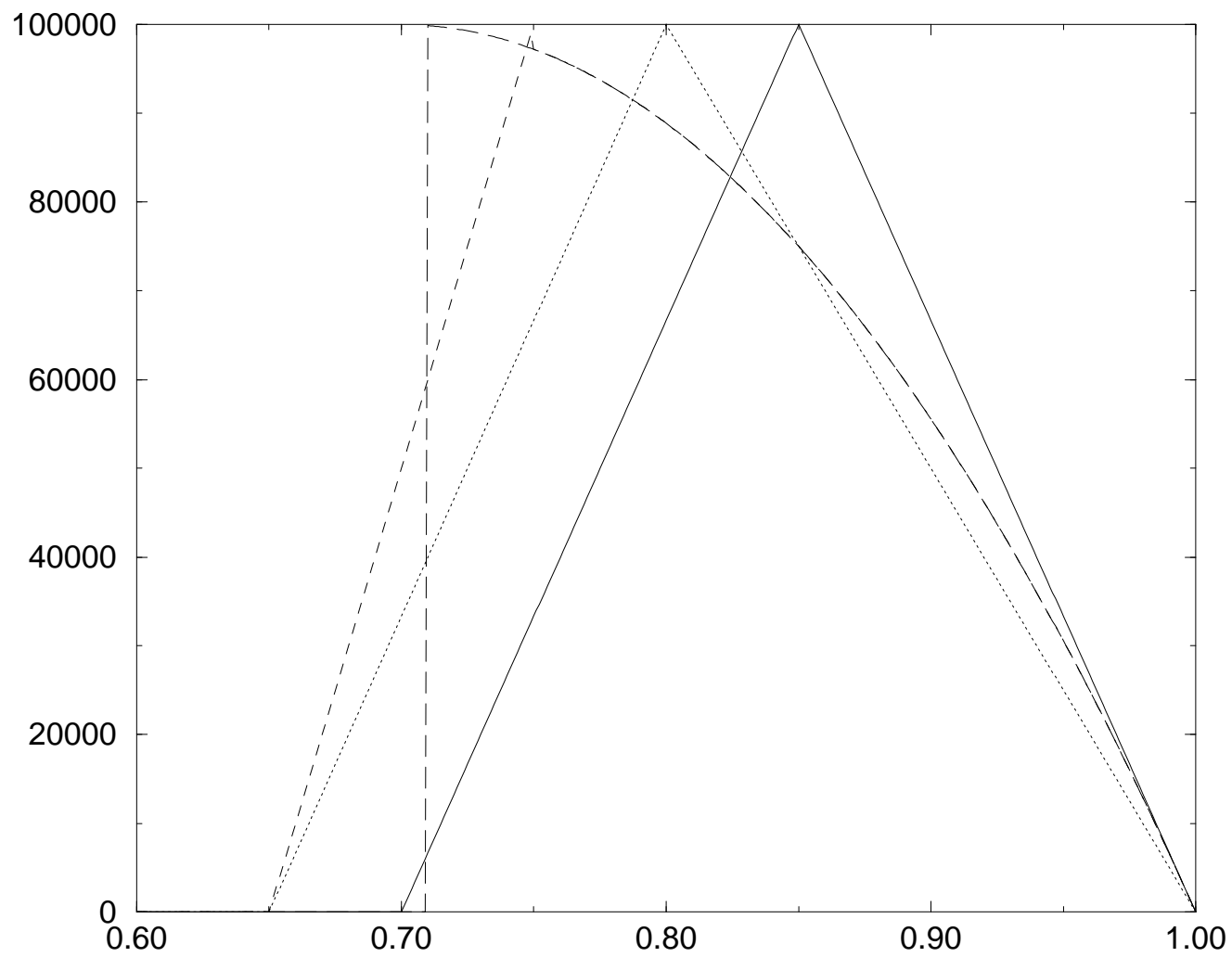
Fig. 10. Rate fits: $\chi^2/d.o.f.$ as a function of the peak field for several values of Δm_{21}^2 (profile 6). Left: dotted 1.55×10^{-8} eV², full 1.6×10^{-8} eV², short dashed 1.65×10^{-8} eV²,

long dashed $1.70 \times 10^{-8} \text{ eV}^2$, dot-dashed $1.75 \times 10^{-8} \text{ eV}^2$. Right: dotted $1.2 \times 10^{-8} \text{ eV}^2$, full $1.3 \times 10^{-8} \text{ eV}^2$, dashed $1.4 \times 10^{-8} \text{ eV}^2$. Best fit: $\Delta m_{21}^2 = 1.6 \times 10^{-8} \text{ eV}^2$, $B_0 = 9.6 \times 10^4 \text{ G}$, $\chi_{min}^2/d.o.f. = 0.0477$.

Fig. 11. Rate fits: $\chi^2/d.o.f.$ as a function of the peak field (profile 7) for several values of Δm_{21}^2 . Top left: dotted $1.0 \times 10^{-8} \text{ eV}^2$, full $1.1 \times 10^{-8} \text{ eV}^2$, dashed $1.2 \times 10^{-8} \text{ eV}^2$, dot-dashed $1.3 \times 10^{-8} \text{ eV}^2$. Top right: dotted $1.1 \times 10^{-8} \text{ eV}^2$, full $1.2 \times 10^{-8} \text{ eV}^2$, dashed $1.3 \times 10^{-8} \text{ eV}^2$. Bottom left: dotted $1.0 \times 10^{-8} \text{ eV}^2$, short dashed $1.1 \times 10^{-8} \text{ eV}^2$, long dashed $1.2 \times 10^{-8} \text{ eV}^2$, dot-dashed $1.3 \times 10^{-8} \text{ eV}^2$, full $1.4 \times 10^{-8} \text{ eV}^2$. Bottom right: dotted $1.0 \times 10^{-8} \text{ eV}^2$, dot-dashed $1.1 \times 10^{-8} \text{ eV}^2$, full $1.2 \times 10^{-8} \text{ eV}^2$, short dashed $1.3 \times 10^{-8} \text{ eV}^2$. Best fit: $\Delta m_{21}^2 = 1.2 \times 10^{-8} \text{ eV}^2$, $B_0 = 1.66 \times 10^5 \text{ G}$, $\chi_{min}^2/d.o.f. = 0.53$.

Fig. 12. Spectrum fits: for profiles 5 (top) and 6 (bottom) we show the predicted electron recoil spectrum as a function of total electron energy superimposed on data set (II) (825 days), ref. [40], with Δm_{21}^2 and B_0 given by their values corresponding to the rates best fits (see figs. 9 and 10). For both, $\chi_{sp}^2/d.o.f. = 23.0/16$, the same as $\chi_{sp_{min}}^2/d.o.f.$ up to three digits. Profiles 5 and 6 (fig. 2) are those providing the best fits for both the rates and spectrum.

Fig. 1.



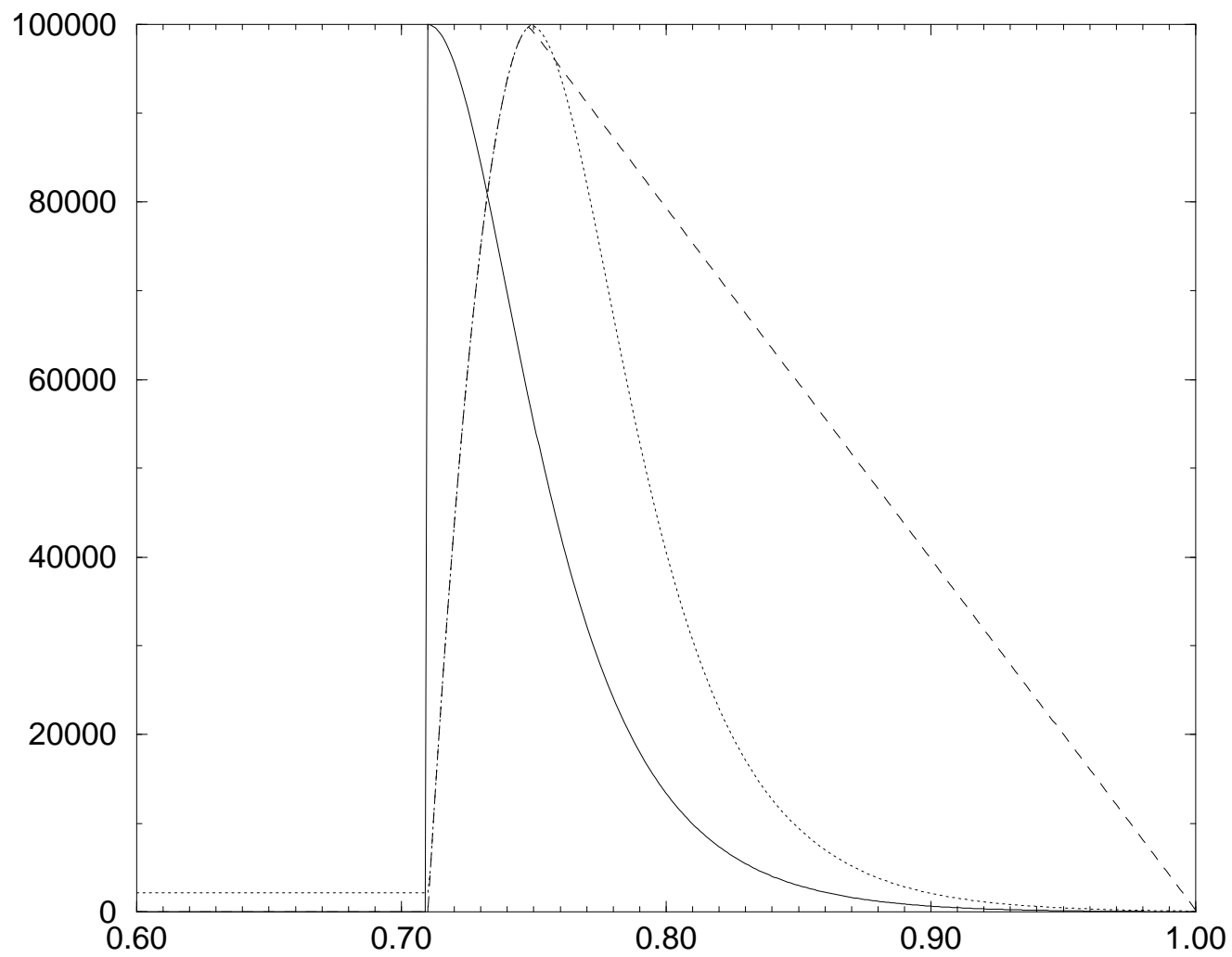


Fig. 2.

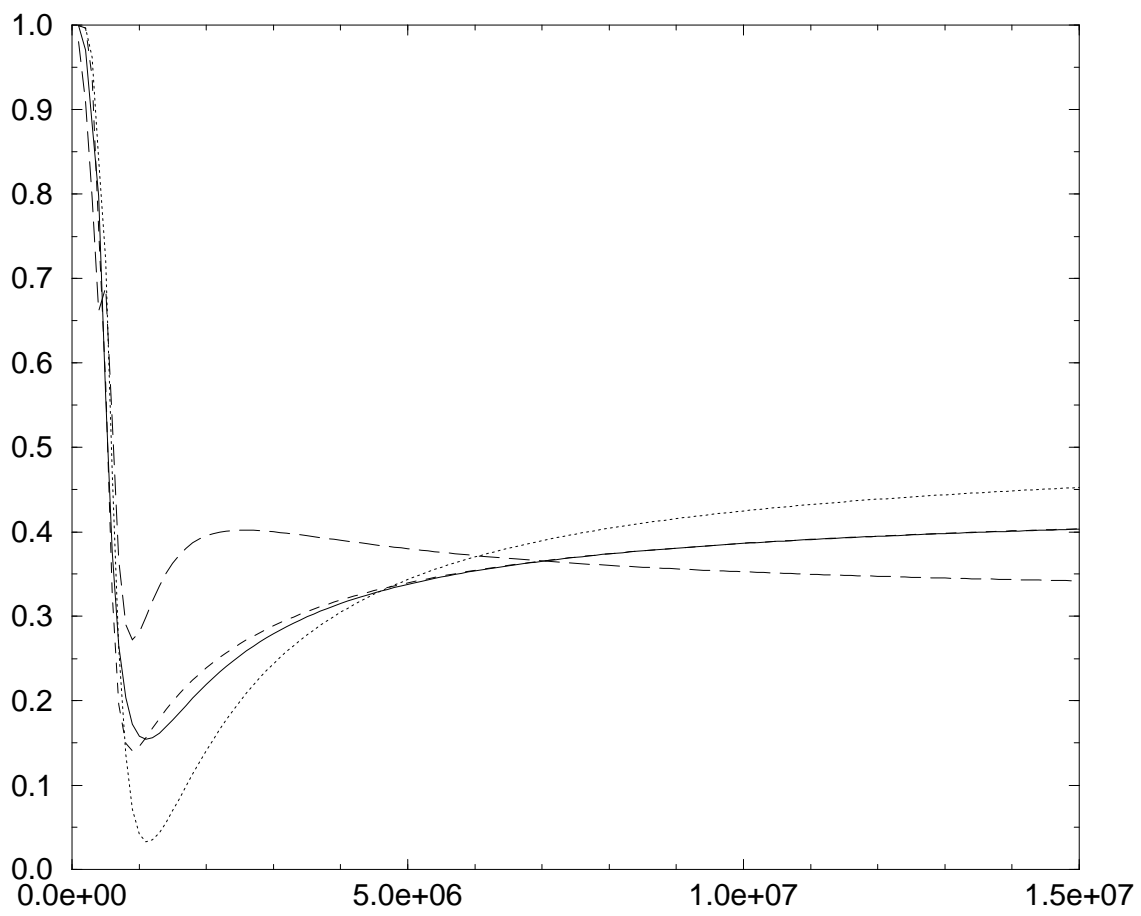


Fig. 3.

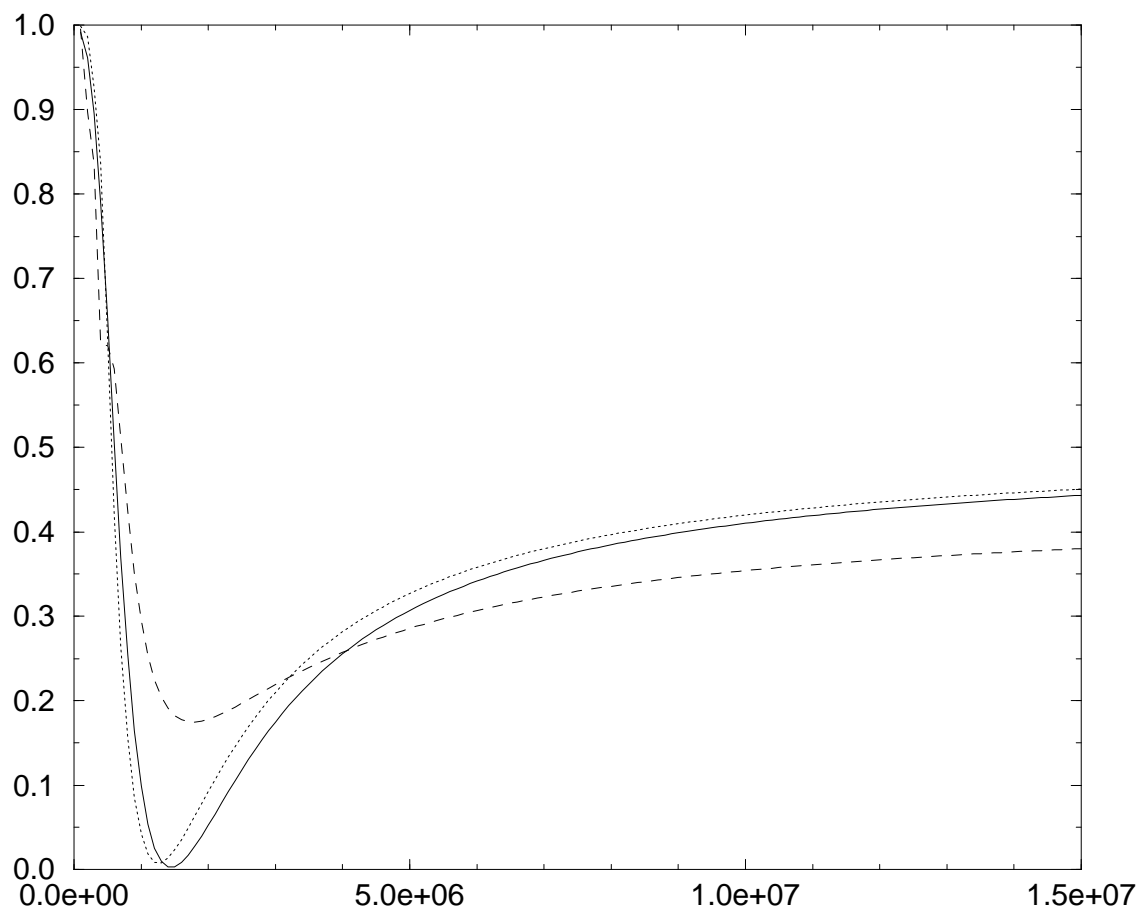


Fig. 4.

Fig. 5.

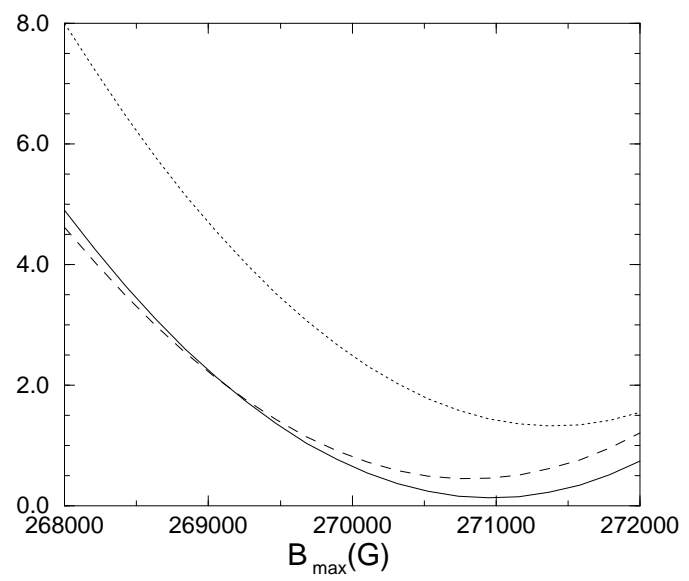
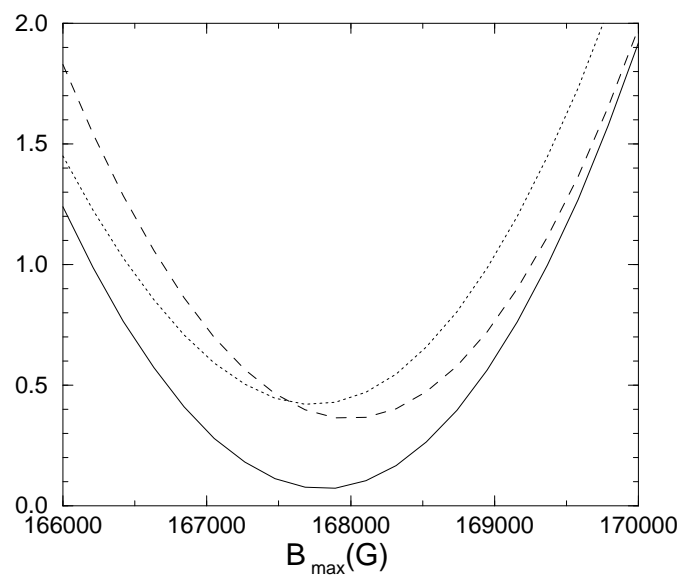
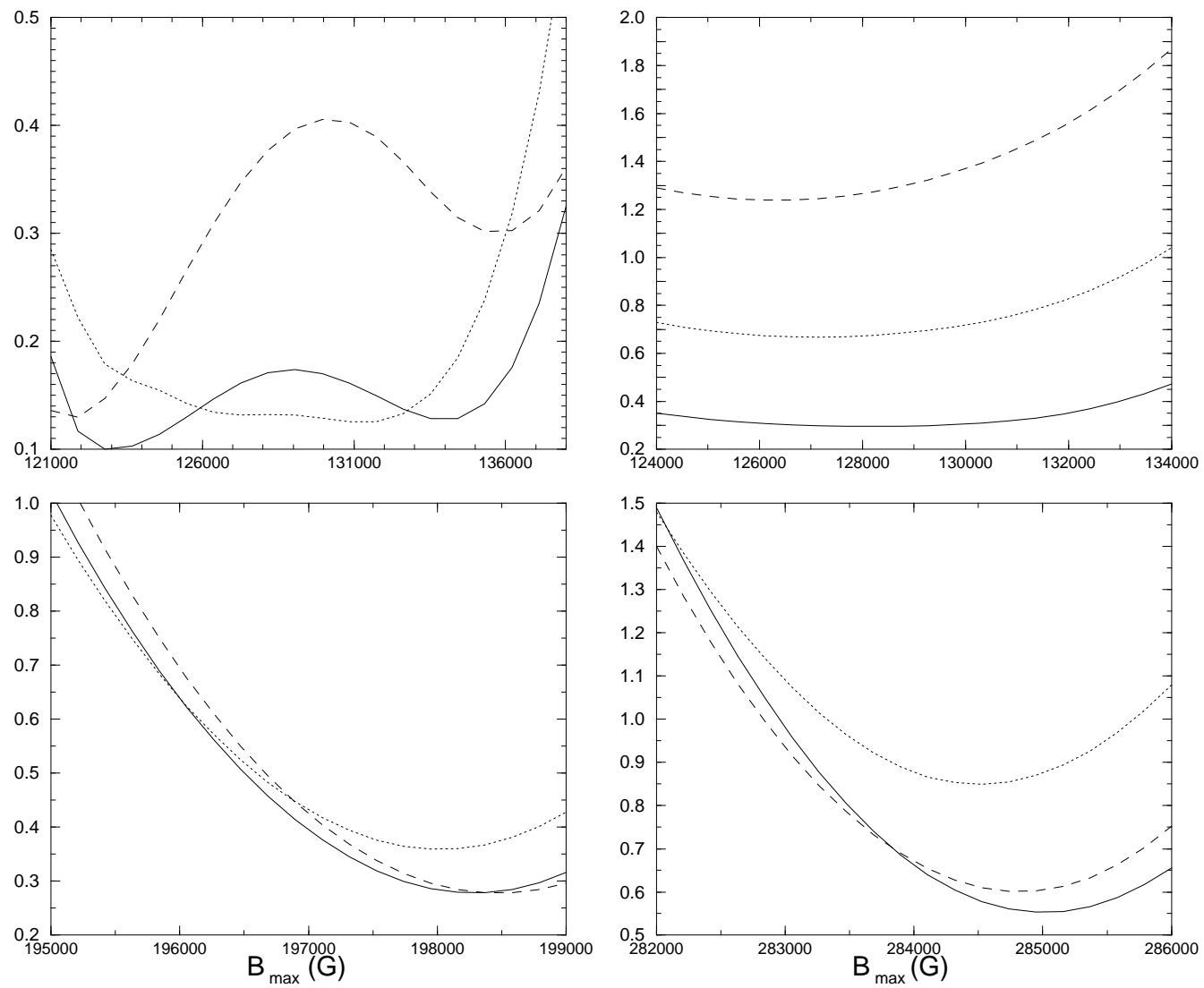


Fig. 6.



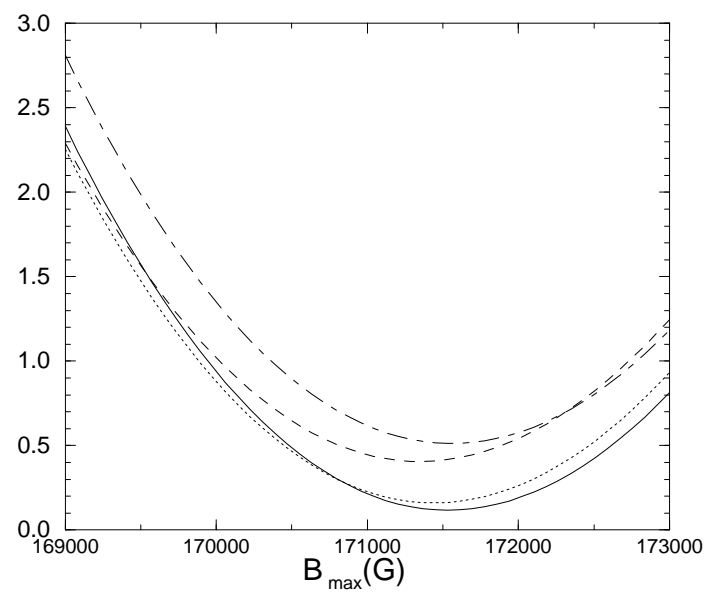
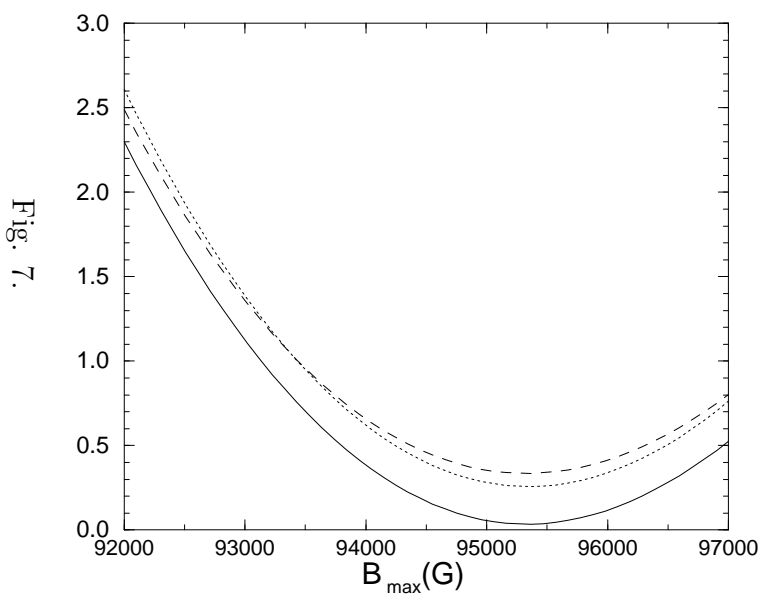
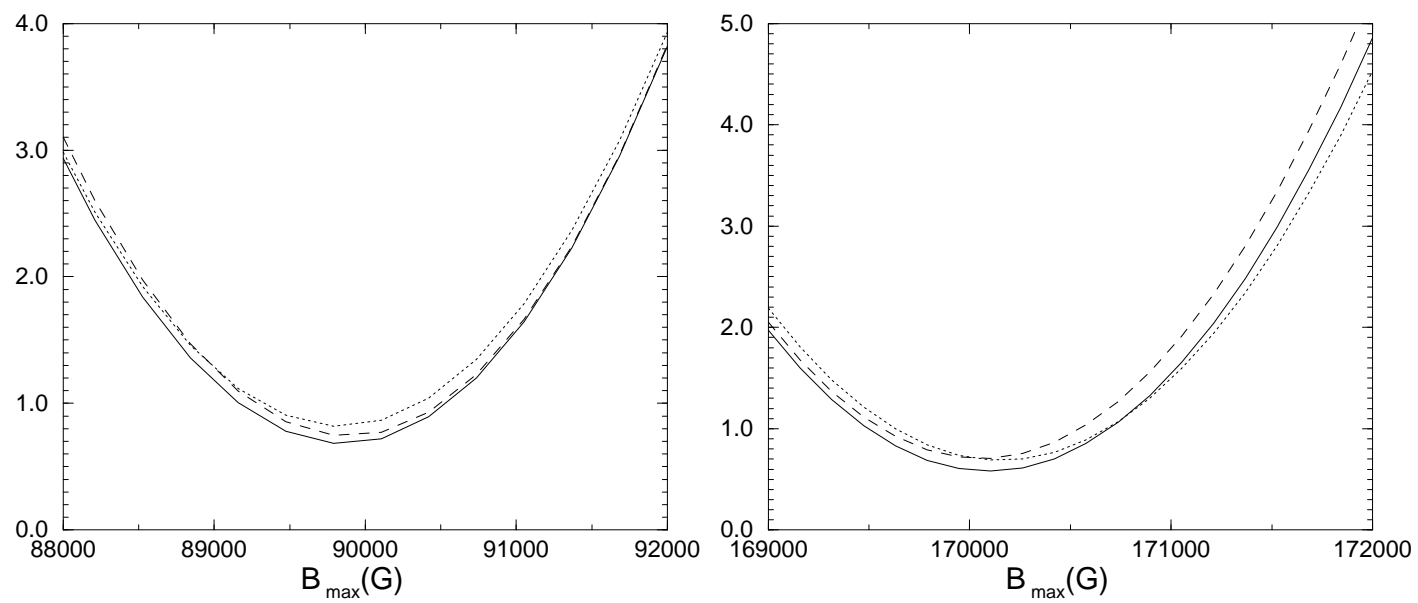


Fig. 7.

Fig. 8.



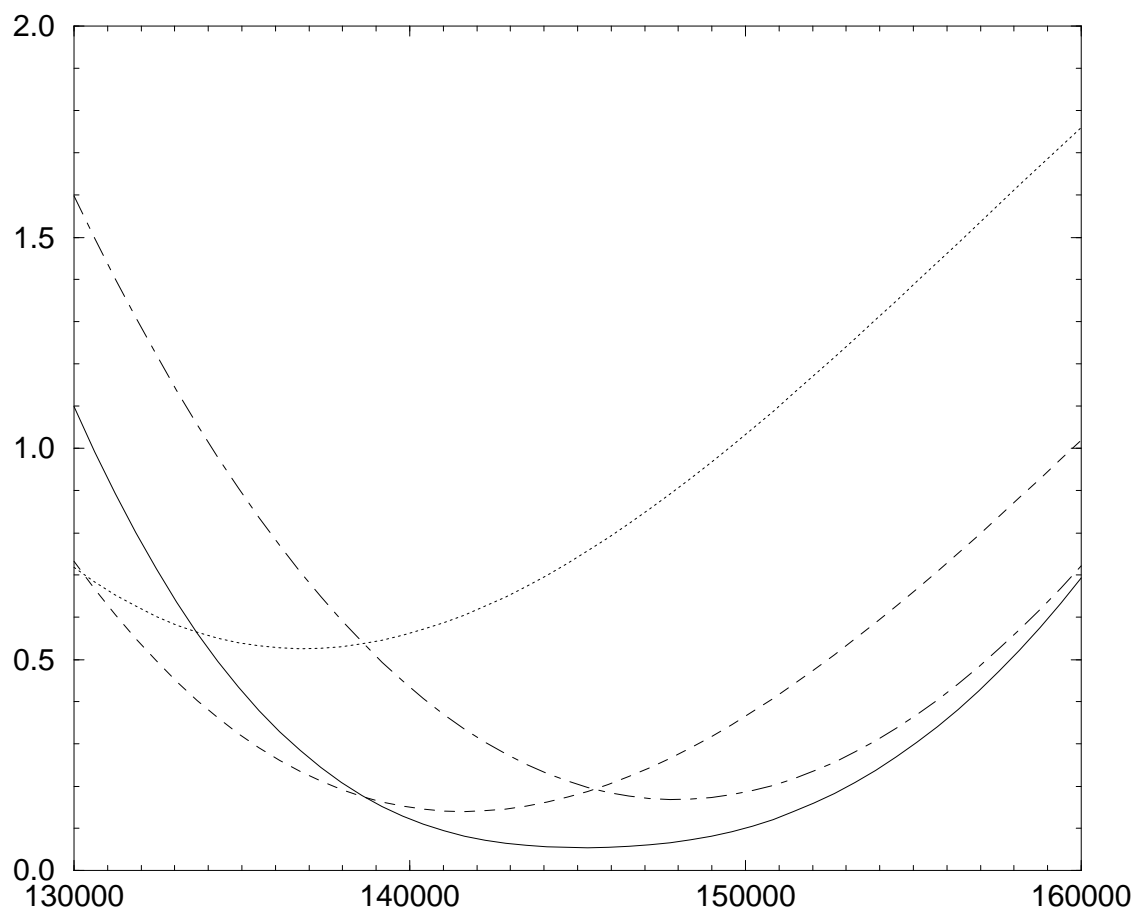


Fig. 9.

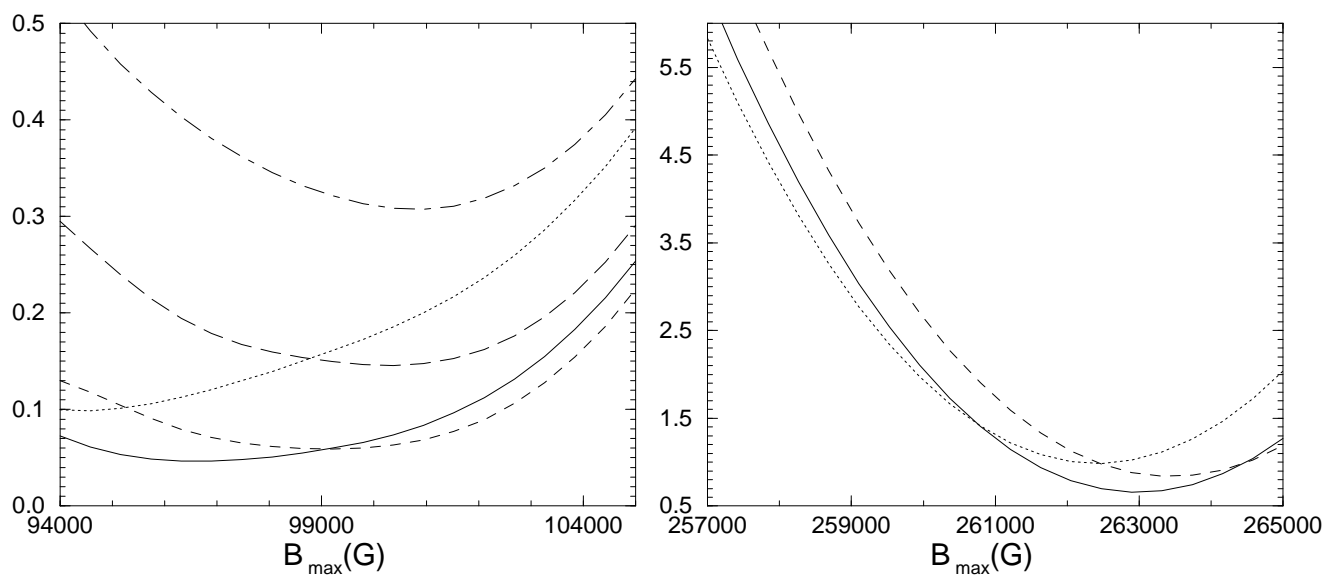
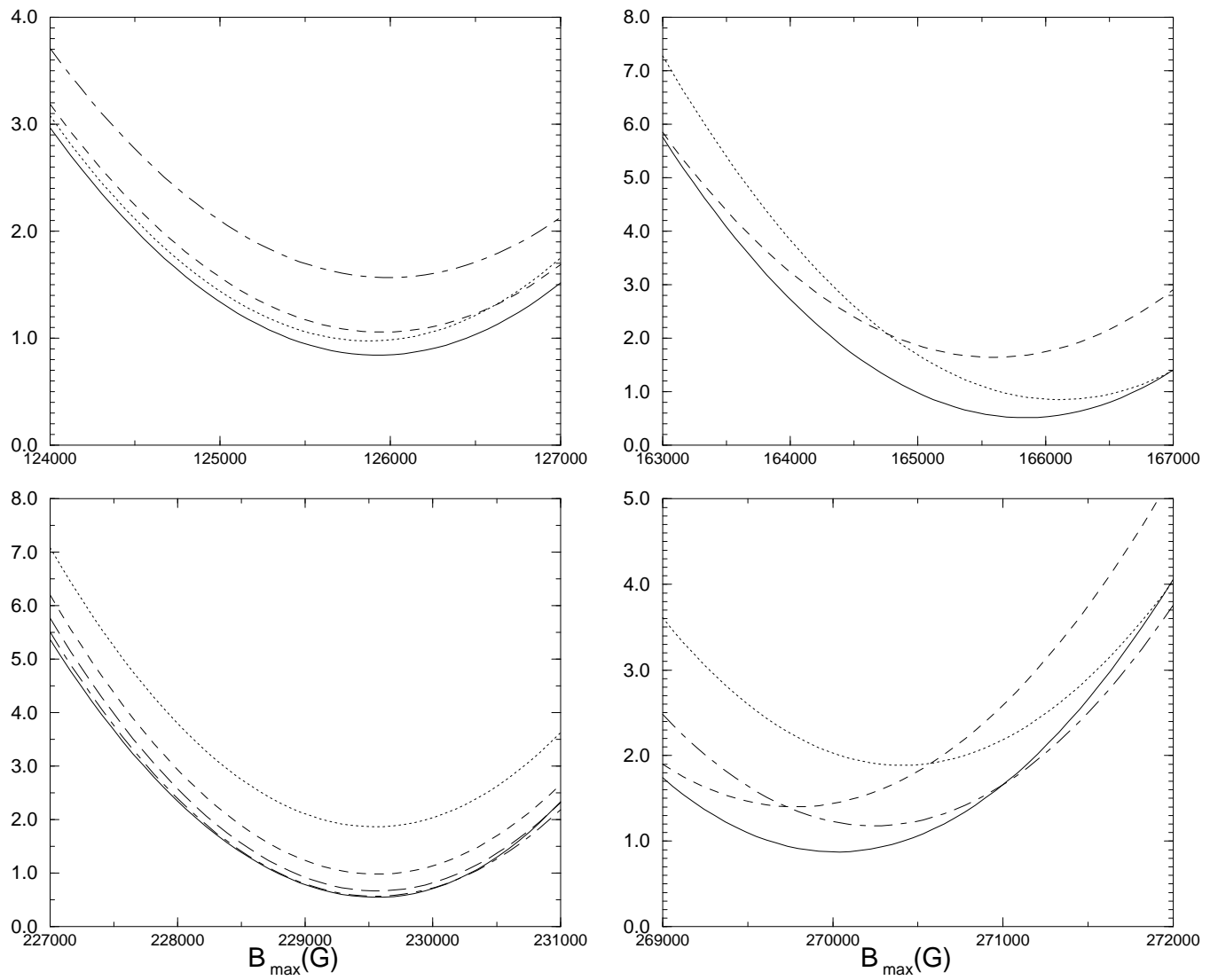


Fig. 10.

Fig. 11.



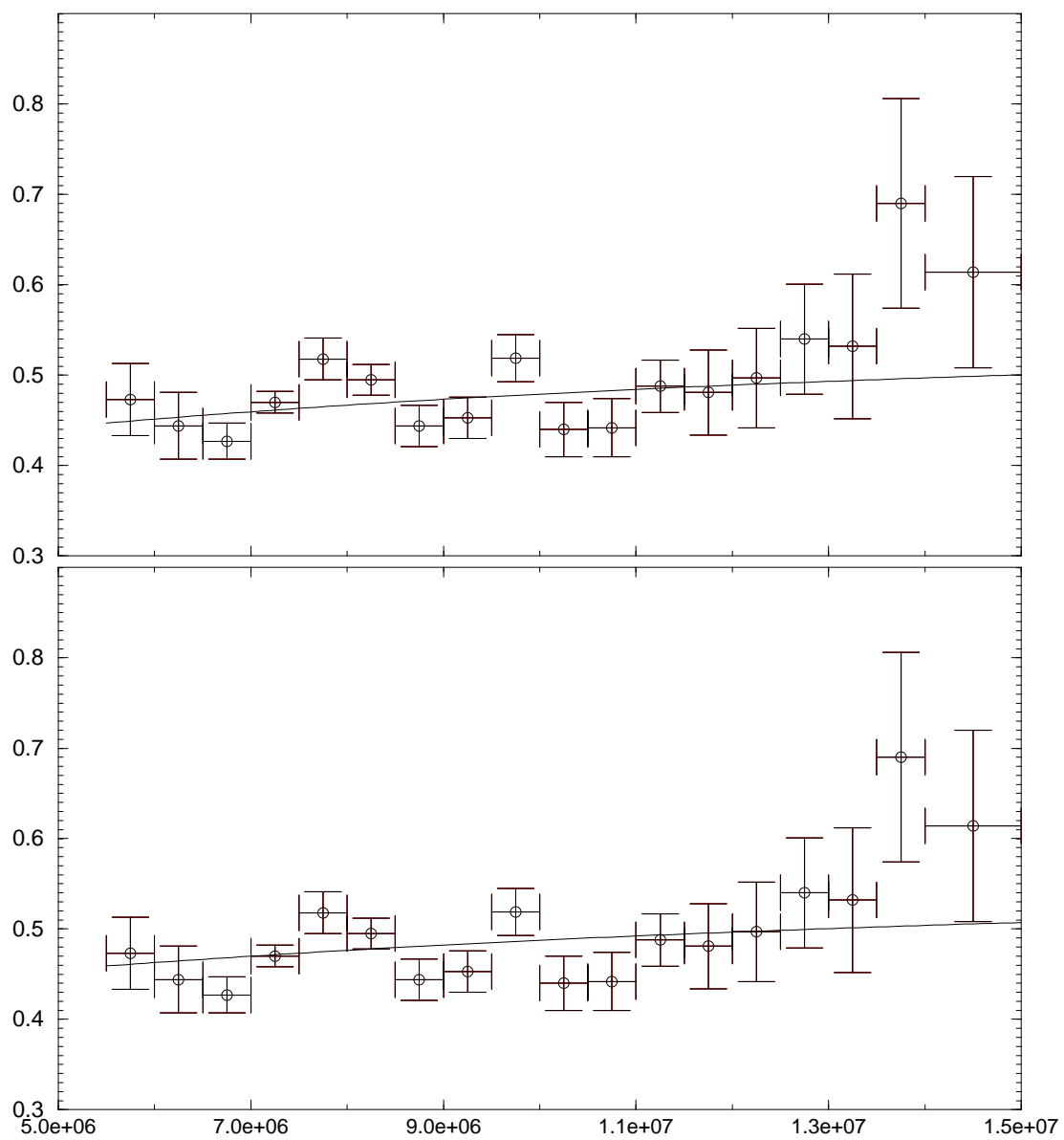


Fig. 12.